PNAS RESEARCH ARTICLE | ENVIRONMENTAL SCIENCES POPULATION BIOLOGY OPEN ACCESS

Southern Ocean seabird population shifts over the Holocene revealed by peat sequestration of mercury from guano

Chuxian Li[a,b,1], Stephen J. Roberts[c], Martin Grosjean[a], Adrien Mestrot[a], Martin Wille[d], Richard A. Phillips[c], Maxime Enrico[e], Kevin Bishop[b], Ulf Skyllberg[f], Dmitri Mauquoy[g], Clemens von Scheffer[g], Thomas Theurer[g], David Muirhead[g], Alex Whittle[c,h], Angela Gallego-Sala[h], Jeroen E. Sonke[i], François De Vleeschouwer[j], Nathalie Van der Putten[k], Pascale Braconnot[l], Olivier Marti[l], Stefan Osterwalder[m], Nina Buchmann[n], Thomas Frölicher[o], Eva Anthamatten[a], Aurea C. Chiaia-Hernández[a], Petra Zahajská[a], Catherine Jeandel[p], Krystyna M. Saunders[q], Sae Yun Kwon[r], Dingyong Wang[s], Richard Bindler[t], Louise Sime[c], and Dominic A. Hodgson[c]

Affiliations are included on p. 9.

Edited by John P. Smol, Queen's University, Kingston, Canada; received November 21, 2025; accepted February 27, 2026

Monitored seabird populations have declined by up to 70% worldwide since the 1950s. Yet, data on long-term seabird population dynamics prior to the anthropogenic era are largely unknown. This limits our ability to understand future population trajectories, particularly in the Southern Ocean, where seabirds are facing multiple environmental threats. Here, we use mercury (Hg) derived from seabird guano in peatland catchments as a tracer of colony population sizes on sub-Antarctic Bird Island (South Georgia). Peat Hg flux and isotope signature results show that the first sustained seabird colonies after deglaciation were established on the island between 6800 and 6100 years ago, predating evidence for colonization on other sub-Antarctic islands by more than 1,000 y. The four subsequent periods with large local seabird populations occurred during phases of less intense Southern Hemisphere westerly winds. Our study unveils significant and repeated millennial-scale shifts in seabird abundance in response to natural climate changes, implying that the present-day increase in westerly wind intensity may lead to further declines in seabird populations in the Southern Ocean.

seabird populations | mercury | Southern Hemisphere westerly winds | Holocene | peat

Significance

The Southern Ocean is home to vast seabird populations and threatened species. To understand the wider impact of the catastrophic decline in many seabird populations over recent decades, we need knowledge of their long-term population dynamics under natural climate variability. We do this by studying mercury flux and stable isotope fingerprints in seabird excrement (guano) that has accumulated in peatland archives around the nest sites. We find that oscillations in peat mercury accumulation reflect guano inputs and therefore seabird abundance. The peat records suggest that seabirds thrived when the Southern Hemisphere westerly winds were less intense. From a past to future perspective, our study indicates that contemporary intensified westerly winds may cause further steep declines in Southern Ocean seabird populations.

Monitored seabird populations have declined globally by ~70% between 1950 and 2010 (1) due to a range of human activities, such as overfishing of food sources, pollution, climate change, and incidental mortality (bycatch) in fishing gear, particularly in the Southern Hemisphere (2). These rapid declines threaten wider ecosystem structure and function, because seabirds provide ecological services, including energy and nutrient transport and cycling (3). Seabirds are also excellent indicators of spatiotemporal changes in marine ecosystem health since they are long-lived, wide-ranging, and forage at high trophic levels (4).

The Southern Ocean is an area of high conservation priority because it is the foraging area for very large seabird populations (5), including many threatened species (2). Numerous Southern Ocean seabird species are likely to decline further in response to future climate change, such as increased sea surface temperature and decreased sea-ice extent that reduce survival rates and breeding performance (6–9). Current monitoring of seabird population sizes and trends largely relies on counts in the field, digital image analysis (from satellites, aircraft, or drones) (10), or acoustic loggers for some burrowing species (11, 12). However, almost all monitoring programs started in the last few decades, and are therefore not able to determine longer-term impacts of natural and anthropogenic drivers. This limits our understanding of preindustrial baselines and ability to develop longer-term (decadal scale) mitigation plans or assess the range of natural pressures on seabird populations.

Biogeochemical analysis of natural archives, such as lake sediments and peat cores, offers opportunities to fill this knowledge gap by providing long-term reconstructions of changing seabird populations (13). Many Southern Ocean seabirds breed on islands where there are lakes, ponds, and peatlands. Seabirds feed on crustaceans (e.g., Antarctic krill, *Euphausia superba*), cephalopods, and fish (14–16), and when back at their breeding and roosting sites excrete guano that is enriched in nutrients and bioelements (e.g., N, C, P, Fe, Cu, Se, Co, Ni, Zn, Mn); these can facilitate plant growth and peat formation (17). Guano can also be transported through runoff and seepage into coastal waters, and lakes, where elements are preserved in sediments (18, 19).

Several studies of lake sediment records from the Northern Hemisphere (13, 20–25) and Antarctica (19, 26, 27) have shown seabird population changes in response to climate,

This article is a PNAS Direct Submission.

[1]To whom correspondence may be addressed. Email: chuxian.li@slu.se.

This article contains supporting information online at https://www.pnas.org/lookup/suppl/doi:10.1073/pnas.2533681123/-/DCSupplemental.

Published April 14, 2026.

ecosystem shifts, explosive volcanism, or anthropogenic influences. For example, geochemical and biomarker methods applied to an 8.5-ka lake sediment profile from Ardley Island revealed that a penguin colony was established following warm conditions on the northern Antarctic Peninsula c. 6.7 ka BP, which is the earliest known for the region (19). Data on seabird population trends prior to the 1950s are limited, and information derived from peat deposits is even rarer, with only three relevant studies available to date (17, 25, 28). Two studies that are largely based on permafrost cores show different timing of seabird presence at different coastal areas in northwest Greenland (25, 28), including the first recorded arrival of the little auk (*Alle alle*) at c. 4.4 ka BP in the Annikitsoq area (25). In the Southern Ocean, a peat core from the east coast of the Falkland Islands indicates colonization by seabirds c. 5 ka BP during a period of regional cooling (17). The past seabird information from all three peat studies largely relies on bioelements (17, 25) and stable isotopes (C, N) (28), in addition to grass pollen and charcoal proxies (17). However, some bioelements might not be widely applicable as tracers for seabird presence in peatland deposits because of their role in metabolism. These bioelements can be recycled by vegetation during peat decomposition, possibly obscuring the signals of guano deposition at the time of peat formation.

Mercury (Hg) is a nonessential trace element that can be a suitable tracer for the incorporation of guano into peat deposits. This element bioaccumulates in marine organisms, and biomagnifies through trophic levels, ultimately reaching high concentrations in top predators such as seabirds (29, 30). Seabird guano input enhances Hg concentrations in peatlands compared to unoccupied sites, leading to high Hg loads at breeding colonies (31–33). For example, a mean total Hg (THg) concentration of 114 ± 50 ng g^{-1} (n = 43) was recorded in deposited guano from a colony of herring gulls *Larus argentatus* on a peatland surface in North America (33). This is three times higher than the mean THg concentration in a remote, uncolonized peatland (37 ± 34 ng g^{-1}, n = 101) (34), which mainly receives Hg from atmospheric deposition. Vegetational sequestration of gaseous element Hg^0, the dominant form of Hg in the atmosphere, is the main deposition pathway of Hg to peatlands in the absence of avian influence (35). Once taken up by vegetation, Hg^0 is oxidized to Hg^{II} via intracellular enzymatic reactions or by reactive oxygen species (36). Rainfall also contributes Hg^{II} to peatlands, but at lower rates [e.g., 20 to 30% of total atmospheric Hg (34, 35, 37)]. Deposited Hg^{II} from rainfall, or produced by oxidation of Hg^0 associated with plant uptake, forms thermodynamically stable complexes with thiol groups of decomposing organic matter in peat, potentially forming immobile nanoparticulate β-HgS (38). The strong affinity of Hg^{II} to organic matter thiols makes it less susceptible to reduction back to Hg^0 (39), thus Hg in peatlands has the potential to reflect input from both the atmosphere and guano (40). Additionally, the Hg stable isotope signatures of atmospheric Hg^0, rainfall $Hg^{II,}$ and guano Hg are distinct (27, 34), enabling identification of Hg input from these sources to peat.

In this study, we apply Hg flux and stable isotope analysis to peatland deposits found on sub-Antarctic Bird Island, a small island at the western end of the South Georgia island group (Fig. 1). South Georgia holds globally important breeding populations of seabirds, including several small but highly abundant burrowing petrel species, as well as albatross, petrel, and penguin species listed as threatened by the *International Union for the Conservation of Nature* because of steep population declines (2, 41). Our main study site at Bird Island, BI10, is a valley peatland that dates back to c. 8.1 ka ago. The BI10 site receives water largely from surface drainage, with a high water table sustained through gravitational lateral seepage from adjacent slopes (42, 43). Guano from seabirds breeding on these slopes is transported from the catchment to the BI10 peatland site. For reference, we investigated changes in Hg at two control sites in the absence of large resident bird colonies: 1) POB4, a highly minerotrophic peatland profile was taken from the Prince Olav Harbour Bog on nearby mainland South Georgia, and 2) FIGG, a peat profile was taken 12 km east of Goose Green on the Falkland Islands. The POB4 profile includes a (lacustrine) sediment sequence at its base and is dated between c. 4.5 to 8.5 ka BP (*SI Appendix*, Supplementary Note 1 and Figs. S1 and S2). All the peat profiles examined in this study were undisturbed and increased in thickness over time, providing a continuous record

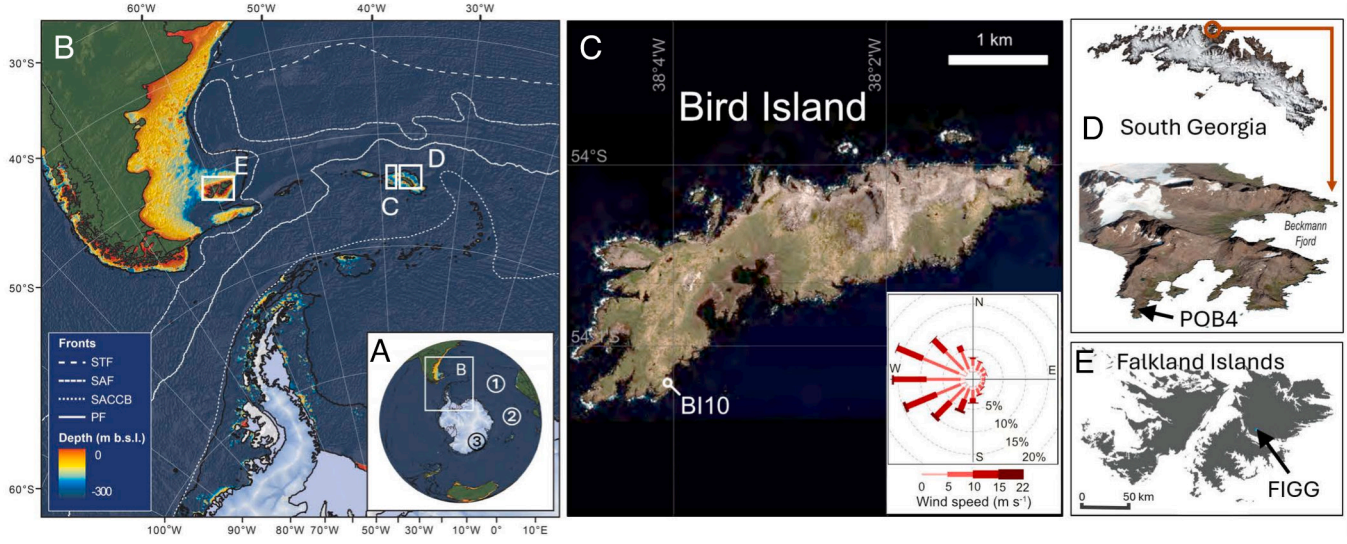

Fig. 1. Locations of the study sites. (*A*) Map of the Southern Hemisphere, highlighting sub-Antarctic regions where peatlands were sampled for this study. ①, ②, ③ show sea-ice records from Nielsen et al. (45), Orme et al. (46), and Röthlisberger et al. (47), respectively. (*B*) Map of the southwest Atlantic sector of the Southern Ocean, showing the locations of the three peatland study sites: Bird Island, South Georgia [*C*, BI10 site, with a wind rose showing wind speed and direction for data averaged from 2012 to 2018 (48)], mainland South Georgia (*D*, POB4 site), and the Falkland Islands (*E*, FIGG site). Major oceanic fronts where seabirds can forage are shown in (*B*), including the Subtropical Front (STF), Subantarctic Front (SAF), Southern Antarctic Circumpolar Current Boundary (SACCB), and the Antarctic Polar Front (PF).

of the environmental conditions prevailing at the time of peat formation (44).

Results and Discussion

Holocene Hg Accumulation Rates At Sub-Antarctic Islands. Over the past 8.1 ka, the mean Hg accumulation rate (HgAR) at Bird Island BI10 was 31.9 ± 18.3 μg m^{-2} y^{-1} (1σ, n = 155, Fig. 2*A* and *SI Appendix*, Table S1), significantly higher than at the control sites at the Falkland Islands FIGG and mainland South Georgia POB4 (two-sample *t* test, $P < 0.01$ for both). BI10 was characterized by prominent fluctuations with a maximum HgAR value of 97 μg m^{-2} y^{-1}. The mean HgAR during the oldest peat formation period at BI10 of 8.1 to 6.8 ka BP was 9.2 ± 3.1 μg m^{-2} y^{-1} (1σ, n = 4). This was followed by an approximately fivefold increase to a mean of 43.2 ± 19.0 μg m^{-2} y^{-1} (1σ, n = 7) from c. 6.8 to 6.1 ka BP, and four other prominent HgAR peaks of up to a millennium in duration in more recent years; 5.2 to 3.5 ka BP, 2.7 to 2.1 ka BP, 1.4 to 1.2 ka BP and 0.5 to 0.1 ka BP, with HgAR of 48.3 ± 18.2 (1σ, n = 28), 45.8 ± 12.2 (1σ, n = 30), 50.0 ± 21.1 (1σ, n = 6) and 26.7 ± 6.1 μg m^{-2} y^{-1} (1σ, n = 15), respectively (Fig. 2*A*).

In contrast, HgAR at the control site FIGG ranged from 1.1 to 5.9 μg m^{-2} y^{-1}, with a mean of 2.2 ± 1.1 μg m^{-2} y^{-1} (1σ, n = 33; *SI Appendix*, Table S2). This mean is lower than that in the mainland South Georgia POB4 profile, which was 6.0 ± 3.9 μg m^{-2} y^{-1} (1σ, n = 74, two-sample *t* test, $P < 0.01$, Fig. 2*A* and *SI Appendix*, Table S3). Both FIGG and POB4 receive Hg predominantly from the atmosphere by vegetation uptake of Hg^0 and rainfall supply of Hg^{II} (35). The mean HgAR at both FIGG and POB4 is comparable to global natural background levels for peat (4.5 ± 3.2 μg m^{-2} y^{-1}, 1σ, n = 17 peat cores) (50).

Holocene HgAR was significantly higher at BI10 than at FIGG and POB4, implying an additional, predominant source of Hg at the BI10 site (Fig. 2*A*). This was also reflected in the BI10 Hg/C

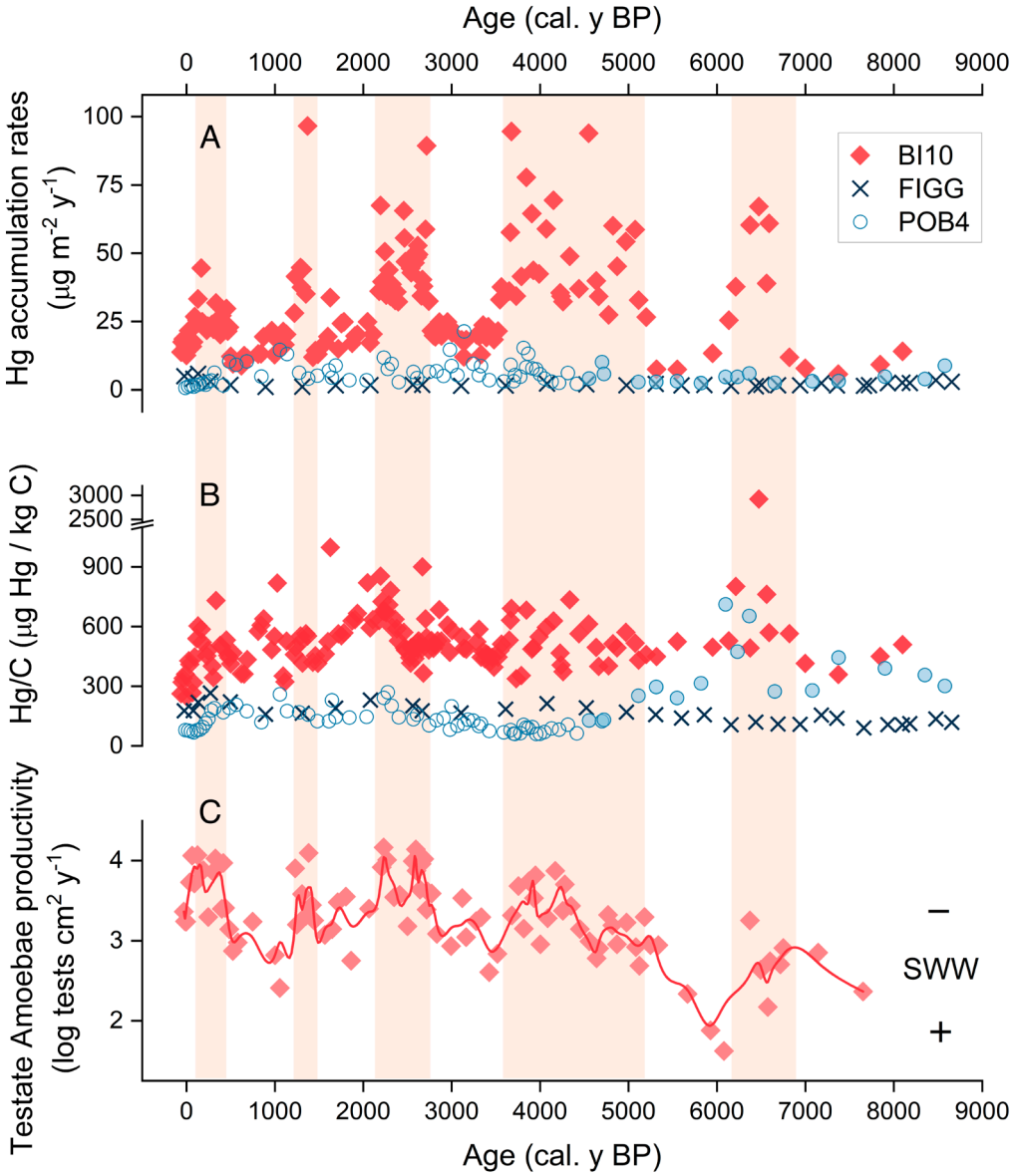

Fig. 2. Profiles of Hg accumulation rates, Hg/C, and testate amoebae productivity. (*A*) Hg accumulation rates in peat cores at Bird Island, South Georgia (BI10, diamonds), Falkland Islands (FIGG, crosses), and mainland South Georgia (POB4, peat section from 0 to 4.5 ka BP in open circles, sediment section from c. 4.5 to 8.5 ka BP in filled circles). (*B*) Hg/C profiles in BI10, FIGG, and POB4 cores. (*C*) The intensity of Southern Westerly Winds reconstructed from BI10 testate amoebae productivity that is sensitive to wind-blown sea spray (*SI Appendix*, Supplementary Note 2) (48, 49). The red line represents the data smoothed using a 3-point moving average. Orange-shaded areas highlight five periods with high HgAR linked to enhanced guano input.

profile (Fig. 2*B*), which normalizes Hg accumulation for changes in peat carbon accumulation. BI10 Hg/C shows a broadly increasing trend during the periods of high HgAR, suggesting excess Hg inputs compared to the FIGG and POB4 sites (Fig. 2*B*). BI10 Hg/C was at least three times higher than that in the FIGG and POB4 peat cores (to c. 4.5 ka BP in POB4; *SI Appendix*, Supplementary Note 1), even though the mean percentage of carbon in the BI10 peat (39.0 ± 5.8%, 1σ; n = 155) was not significantly different from that of POB4 (42.4 ± 6.7%, n = 59, two-sample *t* test, $P > 0.05$) and only slightly lower than FIGG (43% ± 3.70%, n = 65, two-sample *t* test, $P < 0.05$; *SI Appendix*, Tables S1–S3).

The most likely additional source of Hg at BI10 is the input of seabird guano, as this has a very high Hg content (1,200 to 21,600 ng g^{-1}, dry weight, *SI Appendix*, Table S4 and Supplementary Note 3). Seabirds currently breeding in the BI10 catchment at Bird Island include white-chinned petrel *Procellaria aequinoctialis*, wandering albatross *Diomedea exulans*, northern giant petrel *Macronectes halli*, southern giant petrel *Macronectes giganteus*, Antarctic prion *Pachyptila desolata,* and brown skua *Stercorarius antarcticus,* of which the first four species are likely the main sources of guano given their large body sizes and, for white-chinned petrels, also high nesting densities. Seabird guano is known to increase Hg levels in adjacent terrestrial environments (51).

Human activities can be excluded as an important long-term Hg source at BI10, because Bird Island was first discovered in 1775 CE (41), and apart from occasional sealing activities, was occupied intermittently by small numbers of researchers from 1957 until a small permanent research station operated year-round from 1982. Additionally, the substantial difference in HgAR between BI10 and the two control sites cannot be explained by differences in plant species composition (40). All these sites were influenced predominantly by an oceanic cold climate with a vegetation of graminoids, dwarf shrubs, and mosses. The atmospheric Hg pool is also unlikely to be the predominant source for BI10 during the mid to late Holocene because similarly elevated Hg deposition would then have been expected at our control sites, POB4 and FIGG, as the atmospheric Hg pool is relatively well-mixed at hemispheric scales (52). Furthermore, the climate has been comparatively stable over the last c. 8.1 ka, with no dramatic glacial-interglacial scale shifts that could substantially increase (or decrease) regional atmospheric Hg deposition (53). Nor were there periods of very high dust deposition with substantial oxidized Hg, as was the case during the last glacial period (53).

During periods of high Hg flux, the principal climate signal reconstructed from the BI10 peatland site indicated lower intensities of the prevailing Southern Westerly Wind (Fig. 2*C*) (48, 49). The wind intensity was reconstructed from testate amoebae productivity, which is sensitive to wind-blown sea spray (*SI Appendix*, Supplementary Note 2), and is reduced by the input of guano-derived nutrients (54, 55). The pattern of high Hg flux under reconstructed lower wind intensities suggests a potential link between high guano Hg accumulation and a more favorable climate regime for nesting seabirds at Bird Island. Additionally, this link indicates that wind-regulated rainfall may not play a significant role in guano deposition at the peatland site over the long term (i.e., catchment hydrological influence). Lower wind intensity is accompanied by lower humidity and rainfall (34), which could have led to lower guano runoff and Hg deposition in BI10 peat, contrary to the observations. Next, we discuss how Hg stable isotopes can fingerprint seabird guano as the dominant source of Hg in BI10.

Seabird Guano Hg Contribution Constrained By Hg Stable Isotopes. Mercury has seven stable isotopes with masses ranging from ^{196}Hg to ^{204}Hg that can undergo mixing or fractionation via transformation processes (56). Unlike $\delta^{202}Hg$, which represents a typical mass-dependent fractionation (MDF) of Hg isotopes, the odd-mass Hg isotopes can undergo mass-independent fractionation (MIF, $\Delta^{199}Hg$, or $\Delta^{201}Hg$) in specific processes, such as photochemical reactions (56). In contemporary seabird guano collected at Bird Island, $\Delta^{199}Hg$ was 1.32 ± 0.05‰ (1σ, n = 5, *SI Appendix*, Table S4), comparable with penguin guano from the Antarctic Peninsula (0.96 ± 0.03‰, 1σ, n = 2) (27). Regardless of the seabird species and its migration strategy, guano Hg acquires its distinct positive $\Delta^{199}Hg$ from the marine methylmercury (MeHg, organic form of Hg) when marine MeHg is partly degraded by sunlight in ocean surface waters (57). The pool of residual marine MeHg with positive $\Delta^{199}Hg$ subsequently bioaccumulates and biomagnifies in the marine foodweb, leaving its signature in guano, whose Hg is composed of up to 100% of MeHg (33). Guano Hg inputs to peat, therefore, carry distinctly more positive $\Delta^{199}Hg$ than atmospheric Hg inputs to peat (Hg^0 $\Delta^{199}Hg$ = −0.28 ± 0.05‰, 1σ, n = 23; and Hg^{II} $\Delta^{199}Hg$ = 0.21 ± 0.42‰, 1σ, n = 21) (34).

Mean $\Delta^{199}Hg$ at BI10 was 0.61 ± 0.19‰ (1σ, n = 36, Fig. 3*A*), and showed a significant negative relationship with 1/Hg (r = −0.49, linear fit, $p < 0.01$, Fig. 3*B*). This indicates that higher $\Delta^{199}Hg$ is concomitant with higher Hg concentrations at BI10, which is in line with guano $\Delta^{199}Hg$ and Hg concentration signatures. In contrast, the $\Delta^{199}Hg$ at FIGG was negative overall, with a mean of −0.63 ± 0.06‰ (1σ, n = 18) and no significant relationship with 1/Hg (linear fit, $P > 0.05$). The binary source mixing diagram, Fig. 3*B*, showing linearized 1/Hg vs $\Delta^{199}Hg$, indicates that the high Hg concentrations in BI10 can be explained by simple source mixing of guano Hg inputs and atmospheric Hg (manifested as predominant source at FIGG). The $\Delta^{199}Hg$ determined in peatlands worldwide without identified avian influences (34, 37, 58, 59) is generally negative due to the inherently negative $\Delta^{199}Hg$ (−0.28‰) of atmospheric Hg^0 that accumulates in peat. Postdepositional negative shifts in peat soil $\Delta^{199}Hg$ occur due to predominant sulfur-ligand-bound peat Hg^{II} photoreduction (60) or dark abiotic reduction (61), which leaves more negative $\Delta^{199}Hg$ in the peat residue, as observed for FIGG (Fig. 3*A* and *SI Appendix*, Supplementary Note 4). These reduction processes, if they occur, will not cause such a positive $\Delta^{199}Hg$ as recorded at the BI10 site (0.61 ± 0.19‰). Furthermore, as evidenced by the slope of $\Delta^{199}Hg/\Delta^{201}Hg$ as a process indicator, the BI10 peat signature (1.10 ± 0.12, 1σ, Fig. 3*C*) is comparable to that of MeHg in marine biota (∼1.20) (62, 63). Overall, contrasting values of $\Delta^{199}Hg$ between BI10 and peatlands without seabird colonies in the catchment confirm the influence of guano input to the BI10 site.

Similar to $\Delta^{199}Hg$, $\delta^{202}Hg$ in BI10 (−0.79 ± 0.31‰, 1σ, n = 36, Fig. 3*D*), was also significantly higher than in FIGG, which ranged from −2.04‰ to −1.63‰ (two-sample *t* test, $P < 0.01$). Fractionation of $\delta^{202}Hg$ occurs during all physical, chemical, and biological processes (56). At our reference site, the FIGG peat $\delta^{202}Hg$ values show a mean shift of −2.25‰ from the dominant atmospheric Hg^0 sources to peat (Hg^0 $\delta^{202}Hg$ = 0.51 ± 0.16‰, 1σ, n = 23) (34). Low $\delta^{202}Hg$ in FIGG is a result of preferential foliar uptake of light Hg isotopes from the atmospheric gaseous Hg^0 pool (35) (Fig. 3*A*), which is in good agreement with global peatlands (34, 37, 58, 59). Significantly higher $\delta^{202}Hg$ in BI10 than FIGG is most likely due to the input of guano with a high

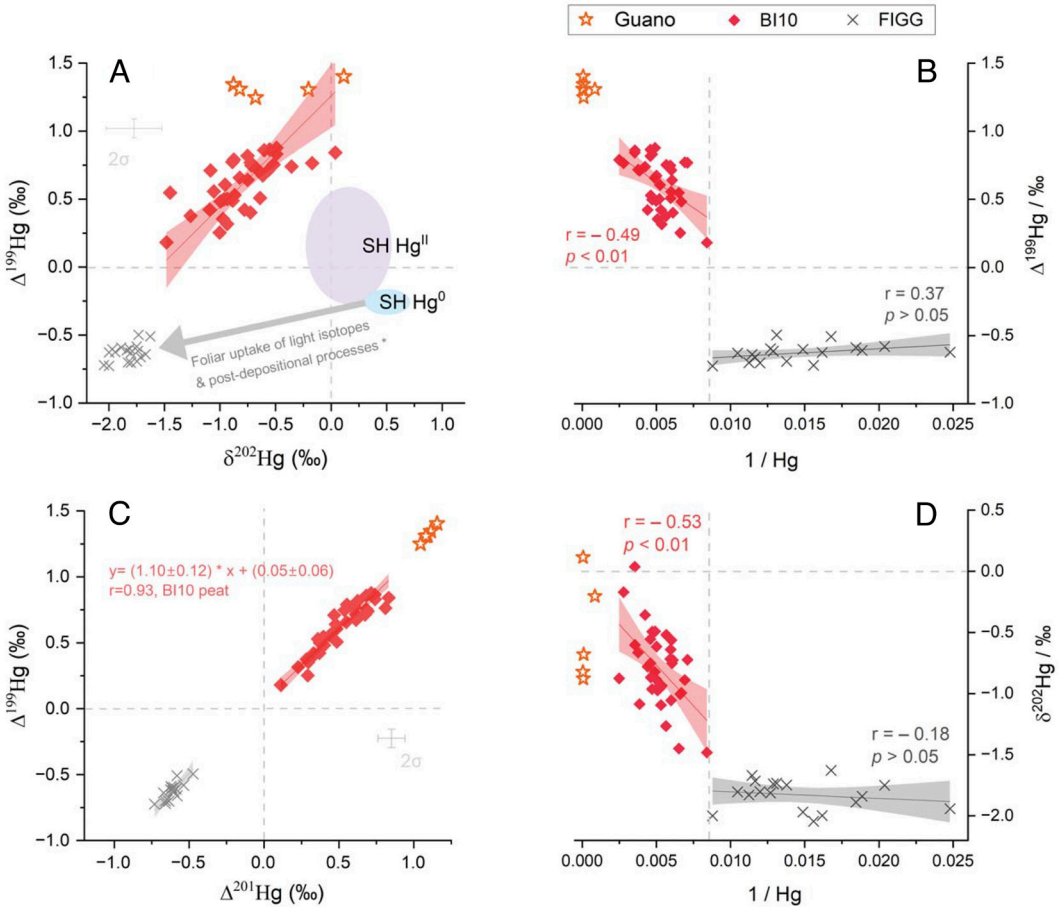

Fig. 3. Hg isotope signatures. (*A*) Δ^{199}Hg vs δ^{202}Hg, (*B*) Δ^{199}Hg vs 1/Hg, (*C*) Δ^{199}Hg vs Δ^{201}Hg, and (*D*) δ^{202}Hg vs 1/Hg in BI10 (red solid diamonds) in comparison to FIGG peat profile (gray crosses) and Bird Island guano (orange open stars). The gray arrow in (*A*) indicates preferential foliar uptake of light isotopes from the Southern Hemisphere atmospheric Hg^0 pool (SH Hg^0, blue filled ellipse), and peat Hg isotope signatures after postdepositional processes on deposited Hg^0 and rainfall Hg^{II} (SH Hg^{II}, purple filled ellipse) (34). The vertical dashed lines in (*B* and *D*) operationally separate 1/Hg above 0.0087 (FIGG data) and below (BI10 data). The red and gray lines in *A*–*D* indicate the linear fit to data from BI10 and FIGG, respectively, and the shaded areas indicate the 95% confidence band.

Hg concentration and a mean δ^{202}Hg value of –0.49 ± 0.39‰ (1σ, n = 5). This is further evidenced in the significant negative correlation between BI10 δ^{202}Hg and 1/Hg (r = –0.53, linear fit, $P < 0.01$, Fig. 3*D*). Additionally, BI10 Δ^{199}Hg and δ^{202}Hg were positively and significantly correlated (r = 0.67, linear fit, $P < 0.01$, Fig. 3*A*), implying that the variability of these two isotope signatures in peat is more driven by Hg sources, rather than postdepositional processes. The important Hg postdepositional processes, such as sulfur-ligand bound peat Hg^{II} photoreduction or dark abiotic reduction (60, 61, 64), generally lead to more negative Δ^{199}Hg and more positive δ^{202}Hg signatures in peat residue, which is contrary to their positive correlation in BI10. Taken together, the peat δ^{202}Hg signature further confirms a dominant guano contribution to the BI10 site.

Guano Nutrient-Fueled Hg Sequestration by Peat Vegetation. In addition to Hg, guano contributes a substantial amount of nutrients (e.g., N, P) to peatland ecosystems, promoting vegetation growth (65). This could be the reason why during c. 8.1 to 0.2 ka BP, carbon accumulation rates in BI10 were 62 ± 33 g C m^{-2} y^{-1} (1σ, n = 143, below water table level), which is 4 times higher than at the FIGG site (12 ± 4 g C m^{-2} y^{-1}, 1σ, n = 54; Fig. S4 and *SI Appendix*, Tables S1–S2) (66). Without substantial avian influence via guano fertilization, long-term carbon accumulation rates on sub-Antarctic Islands are generally low due to the cold climate (67), with multimillennial mean values typically below 20 g C m^{-2} y^{-1} (68). Despite being affected by fire activities (66), FIGG carbon accumulation is comparable to the accumulation rates in other Falkland Islands peat profiles spanning a similar timescale (e.g., mean 19 g C m^{-2} y^{-1} from Whalebone Cove since c. 8.0 ka BP, with 18.73 to 19.34 m^{-2} y^{-1} for 5th to 95th percentile) (68). Peat carbon accumulation rates result from the mass balance between primary production and decomposition loss. Significantly higher carbon accumulation rates at BI10 compared to FIGG could be explained by enhanced primary productivity fueled by guano nutrient input, instead of a lower decomposition rate at BI10. Although nutrient inputs through guano can also facilitate the rates of peat decomposition (68) due to enhanced microbial activities, nutrient-fueled primary productivity at BI10 appears to outweigh higher decomposition rates, ultimately leading to high carbon accumulation rates at the BI10 site. This phenomenon has also been documented in Beauchene Island, the southernmost of the Falkland Islands, where the long-term apparent carbon accumulation rates are also very high (139 g C m^{-2} y^{-1}) (68, 69). N and P fluxes from seabird populations globally are estimated to be 591 Gg N y^{-1} and 99 Gg P y^{-1}, with the highest input in Antarctica and other regions in the Southern Ocean (70). Overall, guano nutrient input promotes peat vegetation growth and carbon sequestration. Enhanced peat vegetation growth presumably leads to increased Hg^0 uptake, hence higher HgAR.

Increased Hg^0 uptake can be examined by the relatively conservative Hg source tracer, even-Hg MIF (represented by Δ^{200}Hg), although it generally has very small variations among sources (56, 71). During high HgAR periods, BI10 peat Δ^{200}Hg is

−0.04 ± 0.03‰ (1σ, n = 20, *SI Appendix*, Fig. S4). These BI10 periods were characterized by lower Δ^{200}Hg values than BI guano Δ^{200}Hg signatures (0.01 ± 0.01‰, n = 5). In contrast, BI10 Δ^{200}Hg values appear to be more commonly associated with atmospheric Hg^0 composition (−0.06 ± 0.02‰, 1σ, n = 23) (34), indicating higher atmospheric Hg^0 sequestration by peat vegetation. Evidence from peat carbon accumulation rates and Δ^{200}Hg suggests two important sources of Hg to the BI10 record, particularly during peak HgAR phases (Fig. 4*A*): elevated Hg directly from guano, and enhanced plant uptake of Hg^0 associated with greater primary production fueled by guano nutrients.

Besides the peak HgAR phases in the BI10 profile, there are five periods with lower HgAR (i.e. c. 8.1 to 6.8, 6.1 to 5.2, 3.5 to 2.7, 2.1 to 1.4, 1.2 to 0.5 ka BP, Fig. 4*A*). A likely explanation for the periods of lower Hg accumulation in BI10 is less guano input linked to lower seabird breeding densities in the peatland catchment. In contrast, photochemical Hg loss from peatlands, which is identified as the main Hg loss pathway (59), is not a primary cause for low Hg accumulation periods at BI10. Because these periods reflect higher wind intensity (Fig. 4*B*) and accompanying increased humidity and cloud cover, which are associated with lower insolation in the study site.

Seabird Establishment and Population Dynamics. High peat HgAR implies more guano input, which we interpret as higher seabird densities in the catchment of BI10 (and vice versa). The peatland formation at BI10 was initiated c. 8.1 ka, likely associated with gradual warming during the early Holocene in the Southern Ocean region (45 to 60°S) (72). At the onset of peat initiation, BI10 was characterized by guano-like positive Δ^{199}Hg and high Hg/C (*SI Appendix*, Fig. S4). This suggests the first colonization of Bird Island by seabirds was around 8.1 ka, but possibly before, and associated with the retreat of glaciers and perennial snow cover. The first period of sustained growth of the seabird colony at BI10 was during c. 6.8 to 6.1 ka, reflected in a pronounced increase in HgAR (Fig. 4*A*). This is in line with the timing of colonization of Antarctic Ardley Island (South Shetland Islands) by penguins (19), but predates other subfossil and geochemical evidence of occupation of the eastern coast of the sub-Antarctic Falkland Islands by at least 1,000 y (17).

Including the colonization at c. 6.8 to 6.1 ka, there were five periods of high Hg fluxes, associated with locally higher seabird abundance (the others were at c. 5.2 to 3.5, 2.7 to 2.1, 1.4 to 1.2, and 0.5 to 0.1 ka; Fig. 4). All five periods are aligned with periods of weaker Southern Westerly Wind intensity (Figs. 4 *A* and *B* and *SI Appendix*, Supplementary Note 2). The Southern Westerly Wind is the strongest time-averaged oceanic wind globally, with a mean annual speed of 9.72 m s^{-1} at Bird Island, dominating its climate (48). Wind regimes affect seabird energy budgets and flight costs, influencing foraging trip durations, chick provisioning rates, breeding success, and hence population dynamics (73). It is possible that the slopes above BI10 became less suitable for nesting during sustained periods of high winds because of increased risk of crash landing, flooding, thermal exposure or, in surface-nesting species, because adults or chicks were blown off their nests, any of which can lead to breeding failure (73). Alternatively, breeding success or recruitment rates of seabirds in the BI10 catchment areas were higher during periods of weaker Southern Westerly Winds. This could arise because of the relationship between wind intensity, marine productivity, and availability of prey for seabirds, which is the main driver of their breeding success and population growth rates in natural situations (74). The four seabird species most likely to be the sources of the guano at BI10 are the white-chinned petrel, wandering albatross, northern giant petrel, and southern giant petrel, which exploit prey over very large areas (75–78). These areas include the Patagonian Shelf and slope, Scotia Arc (including the South Georgia, South Sandwich and South Orkney Islands) and the southern water mass boundary of the Antarctic Circumpolar Current, the Subtropical Front (STF), and the Subantarctic Front (SAF) (Fig. 1*B*). Although these species have diverse diets that may include fish, squid, crustaceans, and carrion, they all exploit the seasonal sea-ice zone at some stage in the breeding season, typically with a lag of several weeks presumably corresponding to the time taken for the spring plankton bloom to transfer energy to mid-trophic-level prey such as squid, fish, or zooplankton (78). For white-chinned petrels and giant petrels, a major component of their diets during chick rearing is Antarctic krill (14, 79); krill feeds on sea-ice algae and is a key species within Southern Ocean food webs (80–82). The extent of the marginal sea-ice zone plays a major role in determining marine productivity and hence in driving changes in breeding success and survival in seabirds.

All five elevated Hg flux phases in BI10 peat occurred during periods of weaker Southern Westerly Wind (Fig. 4*B*) and increased sea-ice extent around the Southern Ocean (Fig. 4 *C*–*E*), so climate and environmental conditions in the Southern Ocean 5,000 y ago may favor seabirds breeding at Bird Island and elsewhere in South Georgia. Between c. 5 to 3.5 ka, seabird densities at BI10 were presumably high for a period of ~1,500 y when sea ice extended to as far north as the Antarctic Polar Front (PF) (Fig. 4 *C*–*E*). At this time, higher prey abundance in the Southern Ocean possibly contributed to the establishment of seabirds or seals breeding at the Surf Bay site on the east coast of the Falkland Islands, as evidenced by marine-derived nutrients from guano facilitating tussac grass establishment and increased peat-forming plant productivity, and increased peat accumulation (17). Overall, our results suggest a strong influence of the Southern Westerly Wind on long-term changes in seabird abundance or distribution, mediated at least in part by its effects on sea-ice extent and marine productivity.

Implications. The Southern Ocean is home to vast seabird populations and many threatened species (83). Currently, knowledge of seabird population response to climate change and anthropogenic pressures is limited largely to the observational period since the 1950s, i.e., recent, decadal timescales. By extending the record of population change back thousands of years, our study has advanced our understanding of how seabird populations have varied on centennial to millennial timescales and how they respond to long-term natural variability in climate and marine ecosystems. This is particularly important because populations of pelagic seabirds have declined dramatically since the 1950s, which must be interpreted both in the context of direct and indirect anthropogenic impacts, including on climate (1, 2). The former includes resource exploitation and bycatch in fisheries (84), pollution (e.g., plastics) (85), and ecosystem impacts of invasive species (predation by mice and rats) (86), while the latter includes intensification and southward displacement of the Southern Westerly Wind (87) and retreat of sea ice in the South Atlantic sector of the Southern Ocean (88). For the climate impacts, this study provides a long-term perspective on which to base more accurate predictions of future changes in seabird populations. These include impacts on breeding success on individual islands as the core belt of the Southern Westerly Wind intensifies and moves southward, and on prey availability in the foraging zone as the sea ice retreats.

By establishing a geochemical framework that can be applied globally, this study opens avenues for understanding how seabird populations respond to climate forcing. We demonstrate that seabird

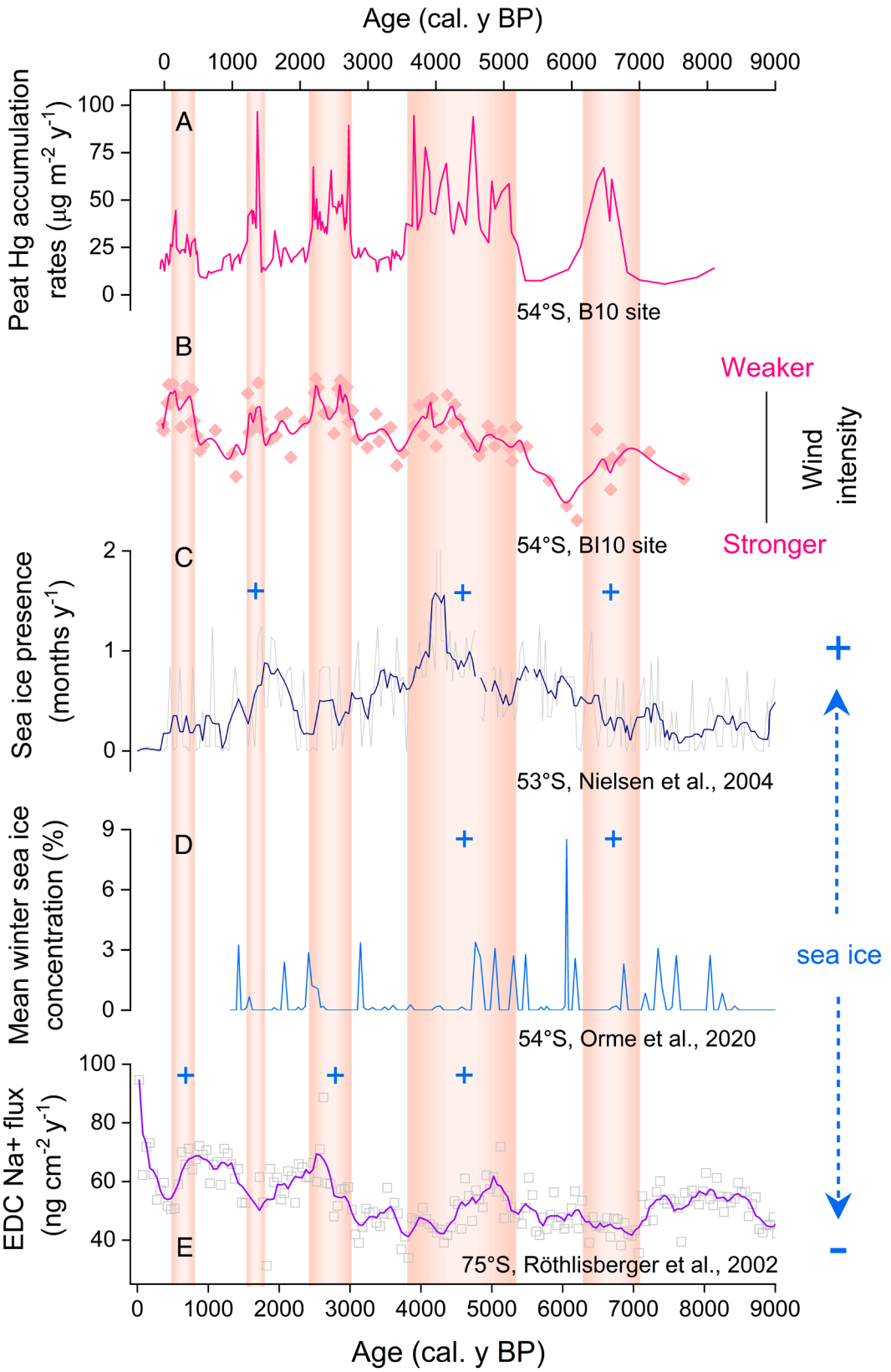

Fig. 4. Southern Ocean seabird population and climate records. (*A*) Hg accumulation rates at BI10 (HgAR, 54 °S, this study). (*B*) Southern Westerly Wind intensity reconstructed by testate amoebae productivity at the BI10 site (48, 49). Image credit: Reprinted form ref. 48. (*C*) Sea-ice presence from the Antarctic Polar Front in the east Atlantic Ocean (53°S, Fig. 1*A*) (45). The dark blue line depicts the results of 3-point smoothing. Image credit: Reprinted from ref. 45. (*D*) Mean winter (September) sea-ice concentrations for core COR1GC (54 °S, Fig. 1*A*) (46). The modern winter sea-ice concentration is marked as 0 as the sea-ice limit is at 59°S. Image credit: Reprinted from ref. 46, which is licensed under CC BY 4.0. (*E*) DOME C sea-salt sodium as a proxy for sea salt (75°S, Fig. 1*A*) (47). Sea-salt concentrations are thought to be influenced by the sea-ice extent and wind speed in the potential source region, as well as the transport from there to the ice core site. The purple line depicts the results of 3-point smoothing. Image credit: Reprinted from ref. 47. Blue crosses indicate enhanced sea-ice cover. Orange-shaded areas highlight five periods with high Hg flux linked to enhanced guano input. -

densities at our study site were negatively associated with the intensity of the Southern Westerly Wind, implying that recent intensification of these winds may have played a role, along with direct anthropogenic impacts, in driving declines in seabird populations in recent decades across the Southern Ocean. Furthermore, our findings underline the threat to seabirds from the recent loss of sea ice in the region. Collectively, this study highlights the need to incorporate the Southern Westerly Wind and sea ice dynamics as climate parameters into demographic modeling to improve the accuracy of seabird population projections. In future research, we may be able to combine the Hg framework used in this study with ancient environmental DNA approaches, which could show presence–absence of each species over time, to identify their millennial-scale population trends under natural climate variability.

Methods

Study Sites and Sampling.

Bird Island. Situated south of the Antarctic Polar Front (Fig. 1*A*), Bird Island is exposed directly to Antarctic storms from the southwest. Gale-force winds can occur all year round. It is cold, cloudy, and wet throughout the year. The mean annual temperature is 1.2 °C, and the annual rainfall is ~850 mm with an average humidity of 84% (89). Temperatures vary from −10 to 10 °C, ~0 °C in winter and ~4 °C in summer, which is characterized by damp, misty, low cloud conditions (89). In winter, the snow cover lasts from July to October, but there is no permanent ice cap, ice, or glaciers on the island, in contrast to mainland South Georgia.

The peat coring site, BI10 (54°01′04.9″S, 38°04′13.7″W), is from a valley floor mire located between the headland at Morris Point and Gony Ridge, surrounded by slopes that are primarily vegetated with tussock grass (*Poa flabellata*) and mosses, including *Chorisodontium aciphyllum* and *Polytrichum alpestre*. The site is approximately 30 m above sea level on the western side of the island and therefore directly exposed to the westerly winds. It receives water largely from surface drainage, with a high water table sustained through gravitational lateral seepage from adjacent slopes (42). The sampled valley mire can, therefore, record guano input through runoff from the surrounding catchment where there are nesting seabirds. The water table level is at 10 to 15 cm below the peat surface.

A 5 m–long peat sequence, selected to be representative of the BI10 site, was collected in Feb 2017 using a 50 × 6 cm Russian corer. Peat cores were described and wrapped in plastic film before placement in PVC tubes and transported to the British Antarctic Survey for frozen storage. Five samples of fresh guano were also collected on Bird Island and stored frozen in plastic tubes.

South Georgia. Located approximately 1,400 km south-east of the Falkland Islands, South Georgia lies between latitudes 54°S and 55°S, and longitudes 36°W and 38°W (Fig. 1*B*). Its climate is typical of the maritime Subantarctic, with annual mean temperatures of 2.0 °C, precipitation of 1,590 mm per year recorded at the research station, King Edward Point (90). Temperatures range from −15 °C to +20 °C (with higher temperatures on the lee side of the mountains enhanced by foehn winds) (90). Snow occurs from May to October. Situated in the northwest of South Georgia, Prince Olav Bog (POB4, 54°04′06″S, 37°06′40″W) is a Sphagnum-dominated peat bog with only 1 to 2 pairs of giant petrels nesting in the catchment (Fig. 1). *Sphagnum fimbriatum* forms dry hummock-like patches, surrounded by wet hollows that are dominated by monocots and brown mosses. A 3.6 m–long peat profile was collected at one of the Sphagnum patches in 2008 using a 50 × 8 cm long Russian peat corer.

Falkland Islands. The Falkland Islands are located between 51°S and 52°30′S and 57° 45′W and 61°30′W. They consist of two large islands (East Falkland, about 6,700 km^2, and West Falkland, about 5,300 km^2), and approximately 700 smaller islands. The archipelago is about 700 km north-east of Cape Horn and 500 km east of the nearest part of the South American continent (Fig. 1). The coring site is ~12 km east of the settlement of Goose Green (FIGG) in an open basin, lying slightly lower than the surrounding hills. The climate is cool maritime, with annual mean temperatures of ~6 °C, precipitation of ~600 mm per year, and a mean wind speed of ~30 km h^{-1} (91).

The coring site, FIGG, is characterized by a typical acid "whitegrass" (*Cotaderia egmontia*) peatland, with *Blechnum penna-marina*, *Baccharis magellanica*, *Empetrum rubrum*, *Oreobolus obtusangulus*, *Gaultheria pumila*, and *Myrteola nummularia*. This site is not currently a nesting ground for seabirds. A 3.6 m-long peat sequence was collected in 2022 using a stainless-steel box of 10 × 10 cm for the top 50 cm of the peat profile, with the remainder sampled using a Russian peat corer with a 50 × 8 cm chamber.

Peat subsampling. Cores were frozen and subsequently sliced at ~1 cm resolution for the whole core. Each new slice was cleaned with MilliQ water, edges removed, and subsampled for further analysis following established protocols (92). The dimension of the largest subsample of each slice was measured using a Vernier caliper to obtain the volume for calculating the dry bulk density and to estimate the cut loss between each slice. Subsequently, the largest subsamples from BI10 and POB4 were dried for geochemical analysis using the freeze-dryers at the University of Toulouse, while those from FIGG were oven-dried at 40 to 50 °C at the University of Aberdeen.

Radiocarbon dating and age models. In total, fourteen plant macrofossil samples from Bird Island BI10, eight from South Georgia POB4, and nine from the Falkland Islands FIGG, were selected for radiocarbon analyses following established protocols (93). All the selected samples were prepared and analyzed for radiocarbon analysis at the University of Aberdeen and the ^{14}CHRONO Centre at Queen's University Belfast, respectively. The age models for BI10 peat profiles, POB4 and FIGG were generated from ^{14}C results using the Bacon model (calibration curve SH Cal20) with the "rbacon" package in R software (https://CRAN.R-project.org/package=rbacon) (94). Details on the dated material and radiocarbon ages from BI10 and FIGG are shown in refs. 48, 66, while POB4 is shown in the *SI Appendix*, Table S5.

BI10 has a chronology of 8.1 ka (*SI Appendix*, Fig. S3). The entire POB4 core is 380-cm long with a chronology of 8.5 ka constrained by eight radiocarbon dates (*SI Appendix*, Fig. S2). This peatland evolved from a lake to a terrestrial environment approximately 4.5 ka ago, resulting in lacustrine sediments between c. 8.5 to 4.5 ka BP followed by peat deposits from c. 4.5 ka BP onward (*SI Appendix*, Supplementary Note 1).

Carbon measurements. Carbon content in BI10 and POB4 was estimated from Loss of Ignition (LOI) at 550 °C, with carbon content estimated as approximately half of LOI (95). Dried peat samples are combusted to ash and carbon dioxide at 550 °C (96). The LOI is then calculated using the following equations:

$$\mathrm{LOI550} = ((\mathrm{DW105} - \mathrm{DW550})/\mathrm{DW}) * 100. \quad [1]$$

Carbon content in FIGG was analyzed using a Flash Combustion Elemental Analyser (CE Instruments NA 2500 Flash Combustion EA) (66). A calibration was performed approximately every 36 to 44 samples, including two blanks and a CRM twice (Hay Powder, BCR-129 with a carbon content of 45.2% for calibration). Every 12 samples, an internal standard was measured (powdered leaf material with a carbon content of 42.6% ± 1.8%, 1σ, based on 80 measurements). Both the LOI and combustion methods for peat carbon content measurement are valid (66, 95, 97).

Hg concentration measurements and Hg accumulation rate calculation. Dried peat and guano samples from BI10, as well as dried peat samples from POB4 and FIGG were analyzed for total Hg concentration on a combustion cold vapor atomic absorption spectrometer (CV-AAS, Milestone DMA-80) at the University of Bern, Switzerland. The analytical performance of the DMA-80 was assessed by multiple measurements on reference material, NIST 1515 (Apple leaves). Results were in good agreement with the certified values, with Hg concentrations of 43.3 ± 2.1 ng g^{-1} (1σ, n = 78, certified 43.2 ± 2.3 ng g^{-1}) for NIST 1515.

Hg flux (μg m^{-2} y^{-1}, Eq. **2**) in sample *i* was obtained by Hg concentration (ng g^{-1}), density (g cm^{-3}), thickness (cm), and age interval (y).

$$\mathrm{Hg\ flux} = \mathrm{Hg\ concentration} \times \mathrm{density} \times \mathrm{thickness/age\ interval}. \quad [2]$$

Hg isotope measurements. Due to sample availability, only BI guano, BI10 peat, and FIGG peat were extracted for Hg isotope analysis using a combustion method adapted from Enrico et al. (98). Hg released from the combustion procedure was collected with 40% inverse *aqua regia* solutions. Following extraction, the Hg stable isotope compositions of guano (5 samples) and peat samples from Bird Island (36) and Falkland Islands (18) were determined from 20% (v/v, diluted from 40%) inverse *aqua regia* solutions using cold-vapor multicollector inductively coupled mass spectrometry (CV-MC-ICP-MS, Neptune Plus, University of Bern). Sample isotopic ratios were corrected for mass bias by sample-standard bracketing using

NIST 3133 (99). Results are reported as δ-values in per mil (‰) representing Hg mass-dependent fractionation by reference to NIST 3133 (Eq. **3**).

$$\delta^{XXX}Hg = \left\{ \left({}^{XXX}H/{}^{198}Hg \right)_{sample} \left({}^{XXX}H/{}^{198}Hg \right)_{NIST3133} - 1 \right\} \times 1000. \quad [3]$$

MIF is calculated based on the deviations of δ-values from the theoretical MDF (Eq. **4**).

$$\Delta^{XXX}Hg = \delta^{XXX}Hg - \beta_{xxx} \times \delta^{202}Hg, \quad [4]$$

where XXX stands for 199, 200, 201, and 204. Symbol β is 0.2520, 0.5024, 0.7520, and 1.493 for ^{199}Hg, ^{200}Hg, ^{201}Hg, and ^{204}Hg, respectively.

The quality control of Hg isotope measurements is assessed by analyzing Almaden, ETH-Fluka, and procedural standards (Apple leaves, NIST 1,515, $n = 35$, *SI Appendix*, Table S6). Almaden showed δ^{202}Hg and Δ^{199}Hg of −0.56 ± 0.13‰ and −0.03 ± 0.07‰ (2σ, $n = 70$), respectively. ETH-Fluka displayed δ^{202}Hg and Δ^{199}Hg of −1.47 ± 0.16‰ and 0.08 ± 0.07‰ (2σ, $n = 9$), respectively. Hg isotopic signatures in procedural standards are reported for δ^{202}Hg (maximum 2σ = 0.25‰), Δ^{199}Hg (maximum 2σ = 0.07‰), Δ^{200}Hg (maximum 2σ = 0.05‰), Δ^{201}Hg (maximum 2σ = 0.09‰), and Δ^{204}Hg (maximum 2σ = 0.17‰). Hg isotope signatures of all three standards are comparable to other published Hg isotope data (59, 100, 101) (*SI Appendix*, Table S6).

Data, Materials, and Software Availability. All study data are included in the article and/or supporting information.

ACKNOWLEDGMENTS. We are very grateful to Manuela Fehr at ETH Zurich, and Christine Alewell and Judith Kobler from the University of Basel, for lending their lab equipment for Hg isotope analysis. We would like to thank Qasid Ahmad for his support with the cup configuration on MC-ICPMS. The study is a contribution to the British Antarctic Survey Polar Science for a Sustainable Planet science strategy funded by the Natural Environment Research Council. This study is largely supported by a Swiss NSF SPF Grant to C.L. (TMPFP2_210183). The MC-ICP-MS at the Institute of Geological Sciences, University of Bern, used in this study was acquired within the framework of the NCCR project PlanetS (Grant nr. 51NF40-141881). A.G.-S. and A.W.'s field work in BI10 was part of the "Late Quaternary changes in the Westerly Winds over the Southern Ocean; the record in sub-Antarctic coastal peatlands" project supported by the British Antarctic Survey (CASS126). D. Mauquoy, C.v.S., and T.T.'s fieldwork was supported by The Leverhulme Trust (Grant number RPG-2020-156).

Author affiliations: [a]Institute of Geography and Oeschger Center for Climate Change Research, University of Bern, Bern 3012, Switzerland; [b]Department of Aquatic Sciences and Assessment, Swedish University of Agricultural Sciences, Uppsala 75007, Sweden; [c]British Antarctic Survey, Natural Environment Research Council, Cambridge CB3 0ET, United Kingdom; [d]Institute of Geological Sciences, University of Bern, Bern 3012, Switzerland; [e]Université de Pau et des Pays de l'Adour, LFCR, E2S UPPA, CNRS, Pau 64000, France; [f]Department of Forest Ecology and Management, Swedish University of Agricultural Sciences, Umeå 901 83, Sweden; [g]School of Geosciences, University of Aberdeen, Scotland, Aberdeen AB24 3U, United Kingdom; [h]Geography Department, University of Exeter, Exeter EX4 4RJ, United Kingdom; [i]Géosciences Environnement Toulouse, Université de Toulouse, CNRS, IRD, Toulouse 31400, France; [j]Instituto Franco-Argentino para el Estudio del Clima y sus Impactos (IRL3351 IFAECI/CNRS-CONICET-IRD-UBA), Universidad de Buenos Aires, Buenos Aires C1428EGA, Argentina; [k]Department of Earth Sciences, Vrije Universiteit Amsterdam, Amsterdam 1081, The Netherlands; [l]Laboratoire des Sciences du Climat et de l'Environnement, LSCE/IPSL, CEA-CNRS-UVSQ, Université Paris-Saclay, Gif-sur-Yvette 91191, France; [m]Department of Geography, Hydrology and Climate, University of Zurich, Zurich 8057, Switzerland; [n]Grassland Sciences, Institute of Agricultural Sciences, ETH Zurich, Zurich 8092, Switzerland; [o]Climate and Environmental Physics, Physics Institute, University of Bern, Bern 3012, Switzerland; [p]LEGOS, Université de Toulouse, CNES, CNRS, IRD, Toulouse 31400, France; [q]Institute for Antarctic and Marine Studies, University of Tasmania, Hobart, Tasmania 7004, Australia; [r]Division of Environmental Science and Engineering, Pohang University of Science and Technology, Pohang, Gyeongbuk 37673, Republic of Korea; [s]College of Resources and Environment, Southwest University, Chongqing 400715, China; and [t]Department of Ecology and Environmental Science, Umeå University, Umeå 901 87, Sweden

Author contributions: C.L. designed research; C.L., S.J.R., M.G., A.M., M.W., R.A.P., M.E., K.B., U.S., Dmitri Mauquoy, C.v.S., T.T., David Muirhead, A.W., A.G.-S., J.E.S., F.D.V., N.V.d.P., P.B., O.M., S.O., N.B., T.F., E.A., A.C.C.-H., P.Z., C.J., K.M.S., S.Y.K., D.W., R.B., L.S., and D.A.H. performed research; C.L., S.J.R., M.G., A.M., M.W., R.A.P., Dmitri Mauquoy, C.v.S., T.T., David Muirhead, A.W., A.G.-S., J.E.S., F.D.V., N.B., and A.C.C.-H. contributed new reagents/analytic tools; C.L., S.J.R., M.W., M.E., Dmitri Mauquoy, C.v.S., A.W., N.V.d.P., S.O., E.A., and D.A.H. analyzed data; S.J.R., M.G., A.M., M.W., R.A.P., M.E., K.B., U.S., Dmitri Mauquoy, C.v.S., T.T., David Muirhead, A.W., A.G.-S., J.E.S., F.D.V., N.V.d.P., P.B., O.M., S.O., N.B., T.F., E.A., A.C.C.-H., P.Z., C.J., K.M.S., S.Y.K., D.W., R.B., L.S., and D.A.H. commented on the manuscript; and C.L. wrote the paper.

The authors declare no competing interest.

1. M. Paleczny, E. Hammill, V. Karpouzi, D. Pauly, Population trend of the world's monitored seabirds, 1950–2010. *PLoS One* **10**, e0129342 (2015).
2. R. A. Phillips, J. Fort, M. P. Dias, "Conservation status and overview of threats to seabirds" in *Conservation of Marine Birds*, (Elsevier, 2023), pp. 33–56.
3. C. J. Whelan, D. G. Wenny, R. J. Marquis, Ecosystem services provided by birds. *Ann. N. Y. Acad. Sci.* **1134**, 25–60 (2008).
4. I. Piatt, W. Sydeman, Seabirds as indicators of marine ecosystems. *Mar. Ecol. Prog. Ser.* **352**, 199–204 (2007).
5. E. A. Pakhomov, C. D. McQuaid, Distribution of surface zooplankton and seabirds across the Southern Ocean. *Polar Biol.* **16**, 271–286 (1996).
6. J. P. Croxall, P. N. Trathan, E. J. Murphy, Environmental change and Antarctic seabird populations. *Science* **297**, 1510–1514 (2002).
7. M. J. Costello *et al.*, "Biodiversity hotspots" in *Climate Change 2022 – Impacts, Adaptation and Vulnerability* (Cambridge University Press, ed. 1, 2023), pp. 2123–2162.
8. S. L. Chown *et al.*, Antarctic climate change and the environment: A decadal synopsis and recommendations for action. *Sci. Comm. Antarct. Res. Camb. U.K.* (2022).
9. C. Barbraud *et al.*, Contrasted demographic responses facing future climate change in Southern Ocean seabirds: Seabird demography and climate change. *J. Anim. Ecol.* **80**, 89–100 (2011).
10. M. R. G. Attard *et al.*, Review of satellite remote sensing and unoccupied aircraft systems for counting wildlife on land. *Remote Sens.* **16**, 627 (2024).
11. S. Oppel *et al.*, Estimating population size of a nocturnal burrow-nesting seabird using acoustic monitoring and habitat mapping. *Nat. Conserv.* **7**, 1–13 (2014).
12. R. T. Buxton, H. L. Major, I. L. Jones, J. C. Williams, Examining patterns in nocturnal seabird activity and recovery across the Western Aleutian Islands, Alaska, using automated acoustic recording. *Auk* **130**, 331–341 (2013).
13. M. P. Duda *et al.*, Reconstructing long-term changes in avian populations using lake sediments: Opening a window onto the past. *Front. Ecol. Evol.* **9**, 698175 (2021).
14. W. F. Mills, T. I. Morley, S. C. Votier, R. A. Phillips, Long-term inter- and intraspecific dietary variation in sibling seabird species. *Mar. Biol.* **168**, 31 (2021).
15. S. D. Berrow, J. P. Croxall, The diet of white-chinned petrels *Procellaria aequinoctialis*, Linnaeus 1758, in years of contrasting prey availability at South Georgia. *Antarct. Sci.* **11**, 283–292 (1999).
16. F. R. Ceia *et al.*, Short- and long-term consistency in the foraging niche of wandering albatrosses. *Mar. Biol.* **159**, 1581–1591 (2012).
17. D. V. Groff *et al.*, Seabird establishment during regional cooling drove a terrestrial ecosystem shift 5,000 years ago. *Sci. Adv.* **6**, eabb2788 (2020).
18. V. Martín-Vélez *et al.*, Quantifying nutrient inputs by gulls to a fluctuating lake, aided by movement ecology methods. *Freshw. Biol.* **64**, 1821–1832 (2019).
19. S. J. Roberts *et al.*, Past penguin colony responses to explosive volcanism on the Antarctic Peninsula. *Nat. Commun.* **8**, 14914 (2017).
20. L. Xu *et al.*, Decline of recent seabirds inferred from a composite 1000-year record of population dynamics. *Sci. Rep.* **6**, 35191 (2016).
21. X. D. Liu *et al.*, Geochemical evidence for the variation of historical seabird population on Dongdao Island of the South China Sea. *J. Paleolimnol.* **36**, 259–279 (2006).
22. M. P. Duda *et al.*, Striking centennial-scale changes in the population size of a threatened seabird. *Proc. R. Soc. B Biol. Sci.* **287**, 20192234 (2020).
23. M. P. Duda *et al.*, Linking 19th century European settlement to the disruption of a seabird's natural population dynamics. *Proc. Natl. Acad. Sci.* **117**, 32484–32492 (2020).
24. M. P. Duda *et al.*, A 2200-year record of Andean Condor diet and nest site usage reflects natural and anthropogenic stressors. *Proc. R. Soc. B Biol. Sci.* **290**, 20230106 (2023).
25. T. A. Davidson *et al.*, The history of seabird colonies and the North Water ecosystem: Contributions from palaeoecological and archaeological evidence. *Ambio* **47**, 175–192 (2018).
26. X. Liu *et al.*, A preliminary record of the historical seabird population in the Larsemann Hills, East Antarctica, from geochemical analyses of Mochou Lake sediments. *Boreas* **36**, 182–197 (2007).
27. W. Zheng, Z. Xie, B. A. Bergquist, Mercury stable isotopes in ornithogenic deposits as tracers of historical cycling of mercury in Ross Sea. Antarctica. *Environ. Sci. Technol.* **49**, 7623–7632 (2015).
28. P. M. Outridge, M. E. Goodsite, O. Bennike, N. Rausch, W. Shotyk, Seabird transfer of nutrients and trace elements from the North Water Polynya to land during the Mid-Holocene Warm Period, Carey Islands, Northwest Greenland + Supplementary Appendix Figure S1 (See Article Tools). *Arctic* **69**, 253 (2016).
29. O. Anderson *et al.*, Influence of trophic position and foraging range on mercury levels within a seabird community. *Mar. Ecol. Prog. Ser.* **375**, 277–288 (2009).
30. W. F. Mills, P. Bustamante, F. Ramírez, M. G. Forero, R. A. Phillips, Mercury concentrations in feathers of albatrosses and large petrels at South Georgia: Contemporary patterns and comparisons with past decades. *Arch. Environ. Contam. Toxicol.* **86**, 363–374 (2024).
31. L. G. Sun *et al.*, Vertebrate records in polar sediments: Biological responses to past climate change and human activities. *Earth-Sci. Rev.* **126**, 147–155 (2013).
32. T. A. Soares *et al.*, Ornithogenic mercury input to soils of Admiralty Bay, King George Island. *Antarctica. Polar Biol.* **47**, 891–901 (2024).
33. H. D. Geizer, S. J. Klapstein, M. L. Mallory, N. J. O'Driscoll, Total mercury, methylmercury, phosphate, and sulfate inputs to a bog ecosystem from herring gull (*Larus smithsonianus*) guano. *Ecotoxicol. Environ. Saf.* **226**, 112845 (2021).
34. C. Li *et al.*, A peat core Hg stable isotope reconstruction of Holocene atmospheric Hg deposition at Amsterdam Island (37.8oS). *Geochim. Cosmochim. Acta* **341**, 62–74 (2023).
35. M. Enrico *et al.*, Atmospheric mercury transfer to peat bogs dominated by gaseous elemental mercury dry deposition. *Environ. Sci. Technol.* **50**, 2405–2412 (2016).
36. Y. Liu *et al.*, Understanding foliar accumulation of atmospheric Hg in terrestrial vegetation: Progress and challenges. *Crit. Rev. Environ. Sci. Technol.* **52**, 4331–4352 (2021), 10.1080/10643389.2021.1989235.
37. G. E. Woerndle *et al.*, New insights on ecosystem mercury cycling revealed by stable isotopes of mercury in water flowing from a headwater peatland catchment. *Environ. Sci. Technol.* **52**, 1854–1861 (2018).

38. V. Liem-Nguyen, U. Skyllberg, E. Björn, Thermodynamic modeling of the solubility and chemical speciation of mercury and methylmercury driven by organic thiols and micromolar sulfide concentrations in boreal wetland soils. *Environ. Sci. Technol.* **51**, 3678–3686 (2017).
39. T. Jiang *et al.*, Modeling of the structure-specific kinetics of abiotic, dark reduction of Hg(II) complexed by O/N and S functional groups in humic acids while accounting for time-dependent structural rearrangement. *Geochim. Cosmochim. Acta* **154**, 151–167 (2015).
40. C. Li *et al.*, Perspectives on using peat records to reconstruct past atmospheric Hg levels. *J. Hazard. Mater.* **482**, 136581 (2025).
41. A. Clarke, J. P. Croxall, S. Poncet, A. R. Martin, R. Burton, Important bird areas: South Georgia. *Br. Birds* **105**, 118–144 (2012).
42. R. I. L. Smith, "Terrestrial plant biology of the sub-Antarctic and Antarctic" in *Antarctic Ecology*, (Academic Press, 1984), pp. 61–162.
43. R. I. Lewis-Smith, Types of peat and peat-forming vegetation on South Georgia. *Br. Antarct. Surv. Bull.* **53**, 119–139 (2019).
44. J. H. C. Fenton, The contribution of Antarctic moss peat to the understanding of global peatland processes. *Antarct. Sci.* **34**, 266–278 (2022).
45. S. H. H. Nielsen, N. Koç, X. Crosta, Holocene climate in the Atlantic sector of the Southern Ocean: Controlled by insolation or oceanic circulation? *Geology* **32**, 317 (2004).
46. L. C. Orme *et al.*, Sea surface temperature in the Indian sector of the Southern Ocean over the Late Glacial and Holocene. *Clim. Past* **16**, 1451–1467 (2020).
47. R. Röthlisberger *et al.*, Dust and sea salt variability in central East Antarctica (Dome C) over the last 45 kyrs and its implications for southern high-latitude climate. *Geophys. Res. Lett.* **29**, 24-1–24-4 (2002).
48. A. Whittle, *Late Quaternary changes in the Westerly Winds over the Southern Ocean* (University of Exeter, 2021).
49. A. Whittle *et al.*, Salt-enrichment impact on biomass production in a natural population of peatland dwelling Arcellinida and Euglyphida (Testate amoebae). *Microb. Ecol.* **78**, 534–538 (2019).
50. C. Li *et al.*, Unequal anthropogenic enrichment of mercury in Earth's Northern and Southern Hemispheres. *ACS Earth Space Chem.* **4**, 2073–2081 (2020).
51. J. C. Kickbush *et al.*, The influence of avian biovectors on mercury speciation in a bog ecosystem. *Sci. Total Environ.* **637–638**, 264–273 (2018).
52. F. Sprovieri *et al.*, Atmospheric mercury concentrations observed at ground-based monitoring sites globally distributed in the framework of the GMOS network. *At. Chem. Phys.* **16**, 11915–11935 (2016).
53. P. Jitaru *et al.*, Atmospheric depletion of mercury over Antarctica during glacial periods. *Nat. Geosci.* **2**, 505–508 (2009).
54. D. Gilbert, C. Amblard, G. Bourdier, A.-J. Francez, The microbial loop at the surface of a peatland: Structure, function, and impact of nutrient input. *Microb. Ecol.* **35**, 83–93 (1998).
55. E. A. D. Mitchell, Response of Testate amoebae (Protozoa) to N and P fertilization in an Arctic wet sedge tundra. *Arct. Antarct. Alp. Res.* **36**, 78–83 (2004).
56. J. D. Blum, L. S. Sherman, M. W. Johnson, Mercury isotopes in Earth and environmental sciences. *Annu. Rev. Earth Planet. Sci.* **42**, 249–269 (2014).
57. B. A. Bergquist, J. D. Blum, Mass-dependent and -independent fractionation of Hg isotopes by photoreduction in aquatic systems. *Science* **318**, 417–420 (2007).
58. M. Enrico *et al.*, Holocene atmospheric mercury levels reconstructed from peat bog mercury stable isotopes. *Environ. Sci. Technol.* **51**, 5899–5906 (2017).
59. C. Li *et al.*, Mercury deposition and redox transformation processes in peatland constrained by mercury stable isotopes. *Nat. Commun.* **14**, 7389 (2023).
60. W. Zheng, H. Hintelmann, Isotope fractionation of mercury during its photochemical reduction by low-molecular-weight organic compounds. *J. Phys. Chem. A* **114**, 4246–4253 (2010).
61. W. Zheng, H. Hintelmann, Nuclear field shift effect in isotope fractionation of mercury during abiotic reduction in the absence of light. *J. Phys. Chem. A* **114**, 4238–4245 (2010).
62. A. Médieu *et al.*, Mercury stable isotopes reveal the vertical distribution and trophic ecology of deep-pelagic organisms over the North-East Atlantic Ocean Continental Slope. *Environ. Sci. Technol.* **58**, 18733–18743 (2024).
63. L. C. Motta *et al.*, Mercury cycling in the North Pacific Subtropical Gyre as revealed by mercury stable isotope ratios. *Glob. Biogeochem. Cycles* **33**, 777–794 (2019).
64. W. Yuan *et al.*, Stable isotope evidence shows re-emission of elemental mercury vapor occurring after reductive loss from foliage. *Environ. Sci. Technol.* **53**, 651–660 (2019).
65. V. R. Smith, Production and nutrient dynamics of plant communities on a sub-Antarctic island: 5. Nutrient budgest and turnover times for mire-grasslands, fjaeldmark and fernbrakes. *Polar Biol.* **8**, 255–269 (1988).
66. C. Scheffer, D. Mauquoy, T. Theurer, D. Coathup, D. Muirhead, 'Fire islands': Holocene wildfire intensity as a critical determinant of carbon accumulation in South Atlantic peatlands. *Quat. Sci. Rev.* **374**, 109759 (2026).
67. A. V. Gallego-Sala *et al.*, Latitudinal limits to the predicted increase of the peatland carbon sink with warming. *Nat. Clim. Change* **8**, 907–913 (2018).
68. R. J. Payne *et al.*, Peatland initiation and carbon accumulation in the Falkland Islands. *Quat. Sci. Rev.* **212**, 213–218 (2019).
69. R. I. L. Smith, R. S. Clymo, An extraordinary peat-forming community on the Falkland Islands. *Nature* **309**, 617–620 (1984).
70. X. L. Otero, S. De La Peña-Lastra, A. Pérez-Alberti, T. O. Ferreira, M. A. Huerta-Diaz, Seabird colonies as important global drivers in the nitrogen and phosphorus cycles. *Nat. Commun.* **9**, 246 (2018).
71. J. Chen, H. Hintelmann, X. Feng, B. Dimock, Unusual fractionation of both odd and even mercury isotopes in precipitation from Peterborough, ON. *Canada. Geochim. Cosmochim. Acta* **90**, 33–46 (2012).
72. M. B. Osman *et al.*, Globally resolved surface temperatures since the Last Glacial Maximum. *Nature* **599**, 239–244 (2021).
73. L. Thorne, T. Clay, R. Phillips, L. Silvers, E. Wakefield, Effects of wind on the movement, behavior, energetics, and life history of seabirds. *Mar. Ecol. Prog. Ser.* **723**, 73–117 (2023).
74. D. K. Cairns, Seabirds as indicators of marine food supplies. *Biol. Oceanogr.* **5**, 261–271 (1988).
75. H. Froy *et al.*, Age-related variation in foraging behaviour in the Wandering Albatross at South Georgia: No evidence for senescence. *PLoS One* **10**, e0116415 (2015).
76. H. M. V. Granroth-Wilding, R. A. Phillips, Segregation in space and time explains the coexistence of two sympatric sub-Antarctic petrels. *Ibis* **161**, 101–116 (2019).
77. R. A. Phillips, J. R. D. Silk, J. P. Croxall, V. Afanasyev, Year-round distribution of white-chinned petrels from South Georgia: Relationships with oceanography and fisheries. *Biol. Conserv.* **129**, 336–347 (2006).
78. E. D. Wakefield *et al.*, Seasonal resource tracking and use of sea-ice foraging habitats by albatrosses and large petrels. *Prog. Oceanogr.* **230**, 103334 (2025).
79. S. E. Thorpe, E. J. Murphy, J. L. Watkins, Circumpolar connections between Antarctic krill (*Euphausia superba* Dana) populations: Investigating the roles of ocean and sea ice transport. *Deep Sea Res. Part I Oceanogr. Res. Pap.* **54**, 792–810 (2007).
80. H. Flores *et al.*, Impact of climate change on Antarctic krill. *Mar. Ecol. Prog. Ser.* **458**, 1–19 (2012).
81. S. Bestley *et al.*, Marine ecosystem assessment for the Southern Ocean: Birds and marine mammals in a changing climate. *Front. Ecol. Evol.* **8**, 566936 (2020).
82. A. S. Brierley *et al.*, Antarctic krill under sea ice: Elevated abundance in a narrow band just south of ice edge. *Science* **295**, 1890–1892 (2002).
83. R. A. Phillips *et al.*, The conservation status and priorities for albatrosses and large petrels. *Biol. Conserv.* **201**, 169–183 (2016).
84. M. A. Collins *et al.*, Mitigating the impact of longline fisheries on seabirds: Lessons learned from the South Georgia Patagonian toothfish fishery (CCAMLR Subarea 48.3). *Mar. Policy* **131**, 104618 (2021).
85. R. A. Phillips, C. M. Waluda, Albatrosses and petrels at South Georgia as sentinels of marine debris input from vessels in the Southwest Atlantic Ocean. *Environ. Int.* **136**, 105443 (2020).
86. A. R. Martin, M. G. Richardson, Rodent eradication scaled up: Clearing rats and mice from South Georgia. *Oryx* **53**, 27–35 (2019).
87. N. C. Swart, J. C. Fyfe, Observed and simulated changes in the Southern Hemisphere surface westerly wind-stress. *Geophys. Res. Lett.* **39**, 2012GL052810 (2012).
88. C. Holmes, E. Doddridge, P. Fretwell, Antarctic Sea Ice #4: Record lows between 2022 and 2025 (2025), https://doi.org/10.48361/KVK6-ZX15.
89. P. Richards, W. Tickell, Comparison between the weather at bird island and King Edward Point, South Georgia. *Br. Antarct. Surv. Bull.* **15**, 63–69 (1968).
90. D. Bannister, J. C. King, The characteristics and temporal variability of föhn winds at King Edward Point, South Georgia. *Int. J. Climatol.* **40**, 2778–2794 (2020).
91. R. G. Scaife *et al.*, The Falkland Islands' palaeoecological response to millennial-scale climate perturbations during the Pleistocene-Holocene transition: Implications for future vegetation stability in the Southern Ocean islands. *J. Quat. Sci.* **34**, 609–620 (2019).
92. F. Vleeschouwer, F. M. Chambers, G. T. Swindles, Coring and sub-sampling of peatlands for palaeoenvironmental research. *Mires Peat* **7**, 1819–754X (2010).
93. D. Mauquoy, B. Van Geel, "Plant macrofossil methods and studies|Mire and peat macros" in *Encyclopedia of Quaternary Science*, (Elsevier, 2013), pp. 637–656.
94. M. Blaauw, J. A. Christen, Flexible paleoclimate age-depth models using an autoregressive gamma process. *Bayesian Anal.* **6**, 457–474 (2011).
95. D. J. Charman *et al.*, Climate-related changes in peatland carbon accumulation during the last millennium. *Biogeosciences* **10**, 929–944 (2013).
96. O. Heiri, A. F. Lotter, G. Lemcke, Loss on ignition as a method for estimating organic and carbonate content in sediments: Reproducibility and comparability of results. *J. Paleolimnol.* **25**, 101–110 (2001).
97. J. S. Bhatti, I. E. Bauer, Comparing loss-on-ignition with dry combustion as a method for determining carbon content in upland and lowland forest ecosystems. *Commun. Soil Sci. Plant Anal.* **33**, 3419–3430 (2002).
98. M. Enrico, P. Balcom, D. T. Johnston, J. Foriel, E. M. Sunderland, Simultaneous combustion preparation for mercury isotope analysis and detection of total mercury using a direct mercury analyzer. *Anal. Chim. Acta* **1154**, 338327 (2021).
99. J. D. Blum, B. A. Bergquist, Reporting of variations in the natural isotopic composition of mercury. *Anal. Bioanal. Chem.* **388**, 353–359 (2007).
100. J. D. Demers, J. D. Blum, D. R. Zak, Mercury isotopes in a forested ecosystem: Implications for air-surface exchange dynamics and the global mercury cycle: Mercury isotopes in a forested ecosystem. *Glob. Biogeochem. Cycles* **27**, 222–238 (2013).
101. T. M. Scanlon *et al.*, Mercury accumulation in tree rings: Observed trends in quantity and isotopic composition in Shenandoah National Park, Virginia. *J. Geophys. Res. Biogeosci.* **125**, e2019JG005445 (2020).